Pergamon

Int. J. Heat Mass Transfer. Vol. 37, No. 3, pp. 375–386, 1994

0017–9310/94 $6.00 + 0.00

Numerical study of thermal convection in tall laterally heated cavities

P. G. DANIELS and P. WANG

Department of Mathematics, City University, Northampton Square, London EC1V 0HB, U.K.

(*Received* 17 *February* 1993 *and in final form* 25 *August* 1993)

Abstract—Two-dimensional convective flows in tall cavities with adiabatic or conducting horizontal boundaries and driven by differential heating of the two vertical sidewalls, are studied numerically over a range of Rayleigh numbers and Prandtl numbers. By using a Dufort–Frankel-Multigrid method, numerical results for the relevant end-zone problems in the limit of large aspect ratio are obtained for a range of Rayleigh numbers from $A = 500$ to 70 000 and for different Prandtl numbers σ. The flow patterns show that the parallel flow in the core region is destroyed at $A_c \approx 7880\sigma$, in good agreement with stability analysis. Nusselt number predictions are compared with those of previous numerical and experimental studies of the overall cavity flow.

1. INTRODUCTION

IN THIS paper, two-dimensional flows driven by horizontal temperature gradients in a tall cavity with adiabatic or conducting boundaries at the top and bottom are considered. The theoretical description of the flow in a vertical slot, based on the Boussinesq approximation, began with the analysis of the conductive regime by Batchelor [1]. The transfer of heat across the cavity by pure conduction leads to a horizontally stratified vertical core flow with a cubic velocity profile corresponding to upward motion in the hotter half of the slot and downward motion in the cooler half. It has been shown (Vest and Arpaci [2], Korpela *et al.* [3], Bergholz [4]) that the flow is unstable to travelling waves for fluids of Prandtl number $\sigma > 12.7$ and to stationary cells for $\sigma < 12.7$. The critical value of the Rayleigh number for stationary instability in the form of transverse rolls is

$$A_c \approx 7.88 \times 10^3 \sigma.$$

Here A is the Rayleigh number based on cavity width and this result is valid for almost the entire range of Prandtl numbers $\sigma > 0$ (Vest and Arpaci [2]). This result is of crucial significance in the description of the base flow in the vertical slot, for when $A > A_c$ the conductive core solution will be destroyed by an imperfect bifurcation associated with the penetration of cells from the end-zones of the slot (Daniels [5]). However, for $A < A_c$, the structure of the flow in the limit of large vertical aspect ratio, $H \to \infty$, has two main parts: a parallel flow in the core region, and nonlinear convective flow near the ends of the slot where the flow must be turned. The end-zone problem first formulated by Daniels [5] contains two parameters, A and σ, instead of the three-parameter problem considered in numerical simulations of the full slot flow by, for example, Lee and Korpela [6]. Daniels discussed various analytical features of the end-zone problem. In particular, it was argued that the break-down of the conductive regime is associated with the inward penetration of nonlinear convective effects from the end-zones. At finite and small Prandtl numbers this takes the form of an imperfect bifurcation at the critical value of the Rayleigh number, A_c, leading to the establishment of a multiple-roll state throughout the slot. For infinite Prandtl number there is a more gradual penetration in which the vertical extent of the end-zones expands as $A \to \infty$, the end-zones eventually filling the entire slot when $A = O(H)$, and leading to the so-called convective regime studied using boundary-layer techniques by Daniels [7]. For the conductive regime where $A = O(1)$ relatively little is known of the detailed flow structure in the end regions, where the full Oberbeck–Boussinesq equations apply. The cavity is assumed to have thermally conducting or insulating horizontal boundaries and the centro-symmetry of the overall flow (Gill [8]) implies that the solution for only one of the end regions needs to be considered.

Here, for the conducting case, complete numerical solutions of the nonlinear end-zone problem are obtained for Rayleigh numbers, A, ranging from 500 to 9000 and for a Prandtl number $\sigma = 0.733$ equivalent to that of air. For the adiabatic case, numerical results are obtained for a wide range of Rayleigh numbers, up to 70 000, and for Prandtl numbers corresponding to air ($\sigma = 0.733$) and water ($\sigma = 6.983$).

Section 2 describes the mathematical formulation of the tall cavity flow, and the core solution in the limit as $H \to \infty$ is given in Section 3. The end-zone problem is also formulated and in Section 4 an efficient numerical scheme of solution is outlined, based on the Dufort–Frankel-Multigrid method, using a finite difference technique. Heat transfer is discussed in

NOMENCLATURE

h	height of cavity	u^*, w^*	dimensional velocity components.
l	length of cavity		
H	aspect ratio of cavity, h/l	Greek symbols	
Nu	Nusselt number	$\tilde{\alpha}$	wavenumber
A	Rayleigh number	β	coefficient of thermal expansion
A_c	critical Rayleigh number	κ	thermal diffusivity
T^*	dimensional temperature	ν	kinematic viscosity
$\bar{T}$, T	non-dimensional temperature	σ	Prandtl number
x^*, z^*	dimensional coordinates	$\bar{\psi}$, ψ	non-dimensional stream function
x, z	non-dimensional coordinates	$\bar{\omega}$, ω	non-dimensional vorticity function.

Section 5. The numerical results and a comparison with theory given in Sections 6–8.

2. FORMULATION

The slot is defined by the region $0 \leqslant x^* \leqslant l$, $0 \leqslant z^* \leqslant h$, with the vertical sidewalls $x^* = 0$ and $x^* = l$ maintained at constant temperatures T_0 and $T_0 + \Delta T$, respectively. Non-dimensional variables of temperature, velocity, length and time are defined by

$$T^* = T_0 + \Delta T \bar{T}(x, z, t), \tag{1}$$

$$(u^*, w^*) = \frac{\kappa(\bar{u}, \bar{w})}{l}, \tag{2}$$

$$(x^*, z^*) = l(x, z), \tag{3}$$

$$t^* = \frac{l^2}{\kappa} t, \tag{4}$$

where κ is the thermal diffusivity.

By introducing a stream function $\bar{\psi}$ such that

$$\bar{u} = \frac{\partial \bar{\psi}}{\partial z}, \quad \bar{w} = -\frac{\partial \bar{\psi}}{\partial x},$$

the governing equations, subject to the Boussinesq approximation, can be written in non-dimensional form as

$$\sigma^{-1}\left(\frac{\partial \bar{\omega}}{\partial t} + J(\bar{\omega}, \bar{\psi})\right) = \nabla^2 \bar{\omega} + A\frac{\partial \bar{T}}{\partial x}, \tag{5}$$

$$\nabla^2 \bar{\psi} = -\bar{\omega}, \tag{6}$$

$$\frac{\partial \bar{T}}{\partial t} + J(\bar{T}, \bar{\psi}) = \nabla^2 \bar{T}, \tag{7}$$

where the Prandtl number σ and the Rayleigh number A are defined by

$$\sigma = \frac{\nu}{\kappa}, \quad A = \frac{g\beta \Delta T l^3}{\kappa \nu} \tag{8}$$

and $\bar{\omega}$ is the vorticity. Here ν is the kinematic viscosity, β is the coefficient of thermal expansion and g is the acceleration due to gravity.

The boundary conditions on the vertical sidewalls are

$$\bar{\psi} = \frac{\partial \bar{\psi}}{\partial x} = 0 \quad \text{on} \quad x = 0, 1, \tag{9}$$

$$\bar{T} = 0 \quad \text{on} \quad x = 0, \tag{10}$$

$$\bar{T} = 1 \quad \text{on} \quad x = 1. \tag{11}$$

In the insulating case, the horizontal boundary conditions are

$$\bar{\psi} = \frac{\partial \bar{\psi}}{\partial z} = 0 \quad \text{on} \quad z = 0, H, \tag{12}$$

$$\frac{\partial \bar{T}}{\partial z} = 0 \quad \text{on} \quad z = 0, H, \tag{13}$$

while if the horizontal surfaces are conducting,

$$\bar{\psi} = \frac{\partial \bar{\psi}}{\partial z} = 0 \quad \text{on} \quad z = 0, H, \tag{14}$$

$$\bar{T} = x \quad \text{on} \quad z = 0, H, \tag{15}$$

where $H = h/l$ is the vertical aspect ratio of the slot.

As noted by Gill [8] the above equations and boundary conditions allow solutions which possess the centrosymmetry properties:

$$\left.\begin{aligned} \bar{\psi}(x, z, t) &= \bar{\psi}(1-x, H-z, t) \\ \bar{T}(x, z, t) &= 1 - \bar{T}(1-x, H-z, t) \\ \bar{\omega}(x, z, t) &= \bar{\omega}(1-x, H-z, t) \end{aligned}\right\} \tag{16}$$

so that in general for the steady-state solution only half of the flow domain needs to be considered; the motion is controlled by the three parameters σ, A and H.

3. CORE SOLUTION AND END-ZONE STRUCTURE

The flow in the slot is characterised by several different regimes which are identified by the relative sizes of the Rayleigh number A and the aspect ratio H, the latter being assumed large. The regime of interest here is that where A is $O(1)$ when the steady-state core flow throughout most of the slot is the conductive

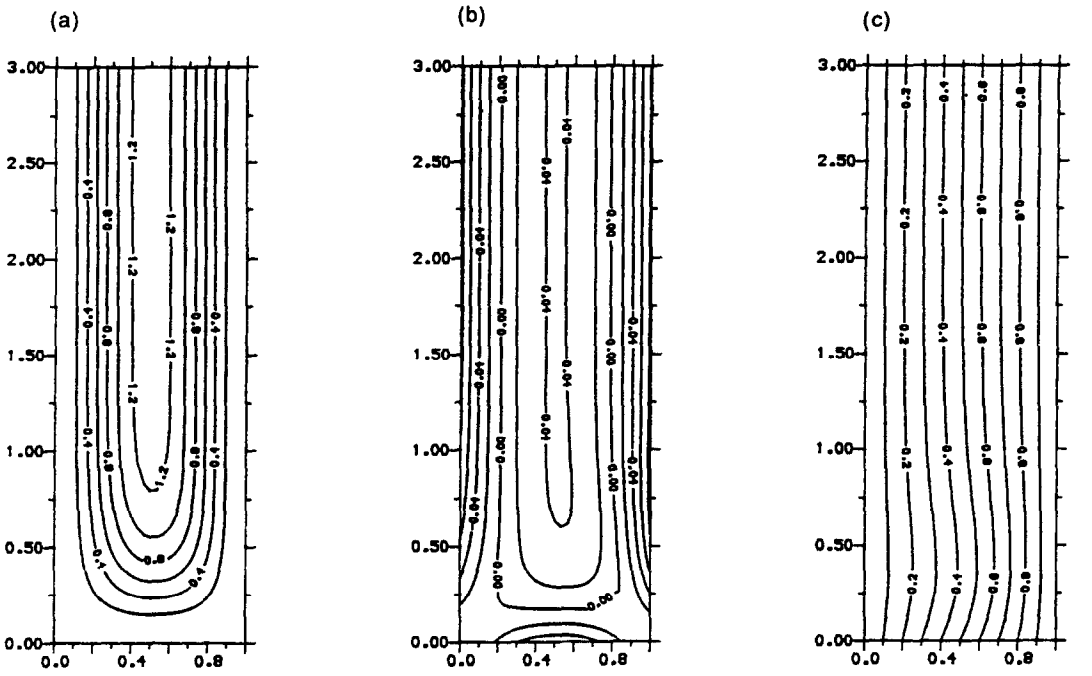

FIG. 1. Contours of the steady-state solution for (a) stream function, (b) vorticity, (c) temperature, for the conducting case with $\sigma = 0.733$ and $A = 500$, using a 30×90 computational grid with $z_\infty = 3$.

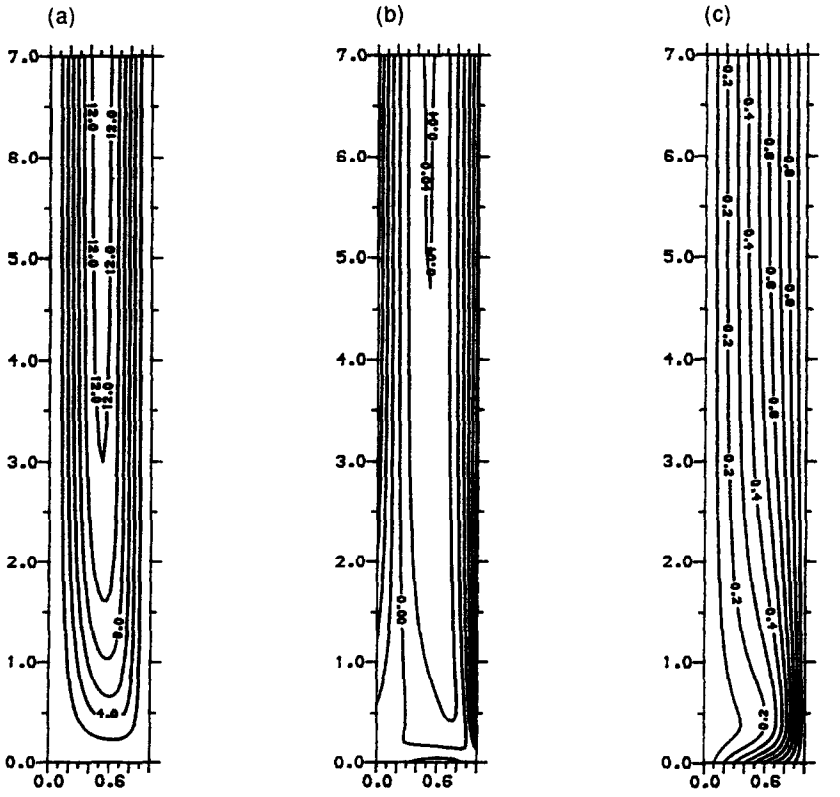

FIG. 2. Contours of the steady-state solution for (a) stream function, (b) vorticity, (c) temperature, for the conducting case with $\sigma = 0.733$ and $A = 5000$, using a 25×175 computational grid with $z_\infty = 7$.

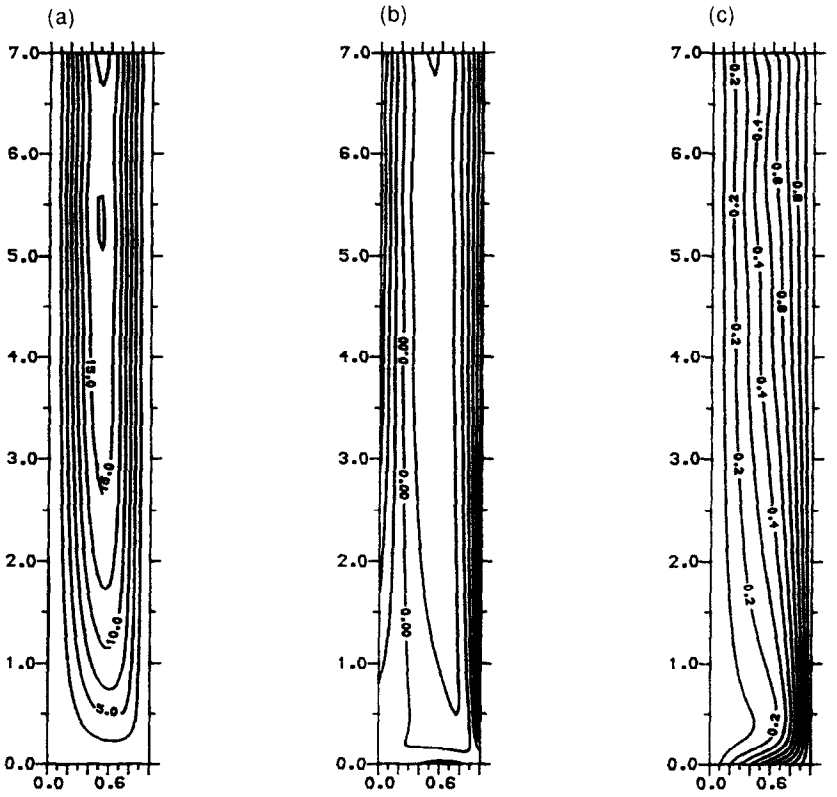

FIG. 3. Contours of the steady-state solution for (a) stream function, (b) vorticity, (c) temperature, for the conducting case with $\sigma = 0.733$ and $A = 7000$, using a 25×175 computational grid with $z_\infty = 7$.

solution

$$\bar{T} = T_c(x), \quad \bar{\psi} = AF(x), \quad (0 < z < H), \tag{17}$$

where

$$T_c(x) = x, \quad F(x) = \frac{x^2}{24}(1-x)^2. \tag{18}$$

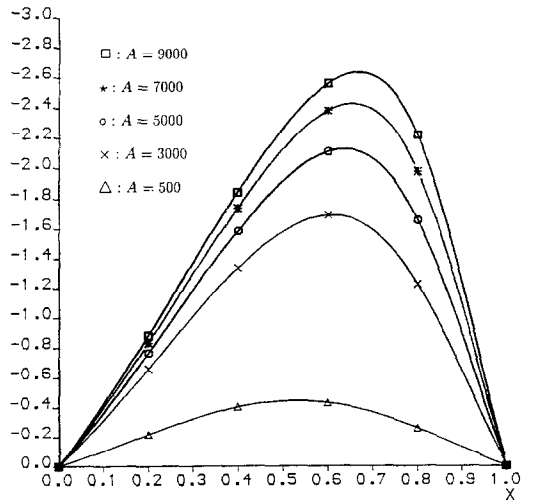

FIG. 4. The local Nusselt number $\partial T/\partial z|_{z=0}$ with $\sigma = 0.733$ for different Rayleigh numbers on the bottom wall for the conducting case.

This solution, originally given by Batchelor [1], is actually an exact solution of the full equations (5)–(7) representing an anti-symmetric vertical motion with fluid ascending in the hotter half of the slot ($x > \frac{1}{2}$) and descending in the cooler half ($x < \frac{1}{2}$). Near the ends of the slot the fluid must be turned and the solution (17) is clearly invalid. Since the overall motion can be assumed centro-symmetric only the solution at the lower end of the slot needs to be considered, and it is clear that if A is of $O(1)$, the motion in an end-zone defined by $0 \leqslant x \leqslant 1$, $0 \leqslant z < \infty$ will be governed by the steady-state version of the full nonlinear Boussinesq equations (5)–(7). It is convenient computationally to consider the time-dependent equations, so the local solution in the end-zone is written

$$\left.\begin{aligned} \bar{T} &= T(x,z,t) + \cdots \\ \bar{\psi} &= \psi(x,z,t) + \cdots \\ \bar{\omega} &= \omega(x,z,t) + \cdots \end{aligned}\right\}, \quad (H \to \infty), \tag{19}$$

and then T, ψ and ω satisfy

$$\sigma^{-1}\left(\frac{\partial \omega}{\partial t} + J(\omega,\psi)\right) = \nabla^2\omega + A\frac{\partial T}{\partial x}, \tag{20}$$

$$\nabla^2\psi = -\omega, \tag{21}$$

$$\frac{\partial T}{\partial t} + J(T,\psi) = \nabla^2 T. \tag{22}$$

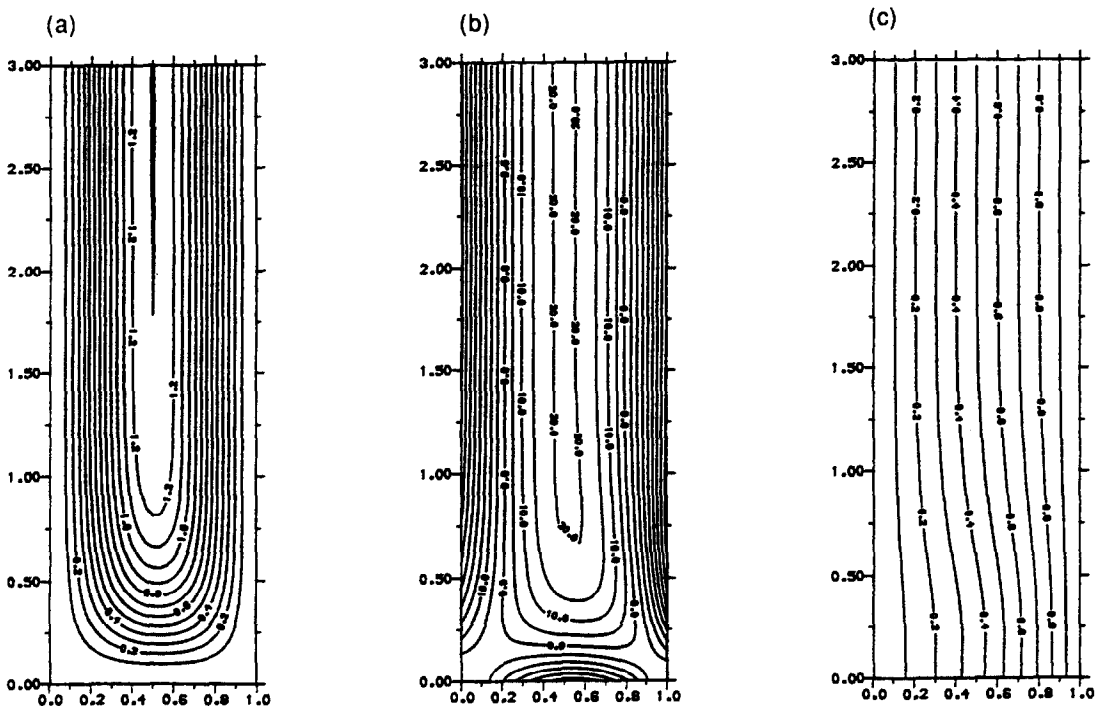

FIG. 5. Contours of the steady-state solution for (a) stream function, (b) vorticity, (c) temperature, for the insulating case with $\sigma = 0.733$ and $A = 500$, using a 30×90 computational grid with $z_\infty = 3$.

The boundary conditions on the rigid cavity walls are

$$\psi = \frac{\partial \psi}{\partial z} = 0, \quad z = 0, \tag{23}$$

$$\psi = \frac{\partial \psi}{\partial x} = 0, \quad x = 0, 1, \tag{24}$$

$$T = 0, \quad x = 0; \quad T = 1, \quad x = 1, \tag{25}$$

and for the insulating case,

$$\frac{\partial T}{\partial z} = 0, \quad z = 0, \tag{26}$$

or for the conducting case,

$$T = x, \quad z = 0. \tag{27}$$

Also as $z \to \infty$ it is required that

$$T \to T_c(x), \quad \psi \to AF(x), \quad (z \to \infty), \tag{28}$$

in order that the solution matches smoothly with that in the core. It is seen that the end-zone problem (20)–(28) is controlled by two parameters, the Rayleigh number A and the Prandtl number σ and that for general values of these parameters in the range $A \geqslant 0$, $\sigma \geqslant 0$ a numerical solution is required. This is discussed in the next section.

4. NUMERICAL APPROACH FOR THE END-ZONE PROBLEM

In order to solve the system (20)–(28) numerically, a finite difference method is considered. In recent years, a scheme called the Dufort–Frankel method, as outlined in ref. [9], has been used frequently for evolution equations. Like Crank–Nicolson and Peaceman–Rachford methods, it has second-order accuracy but since it is an explicit method, it must meet the Courant condition to achieve numerical stability. Although the size of the time step is restricted by this condition, it is still a very effective and fast method. For elliptic equations, a five-point scheme can be adopted in which centred differences are used to approximate the original partial differential equation. Based on this, a new algorithm has been developed recently, called the Multilevel method (Brandt [10]). This is based on the five-point scheme and Successive Over-Relaxation, both widely used for this kind of elliptic equation. The main idea is to use the solution on a coarse grid to revise the required solution on a fine grid. It has been proved theoretically and practically that the Multigrid method has more advantages than other methods, as it has a better rate of convergence. Here we do not give a full theoretical analysis of the algorithm, which is described in detail by Brandt [10].

Here the Dufort–Frankel method is used to solve the evolution equations (20), (22), and the Multilevel method to solve the Poisson equation (21). The outer form (28) at $z = \infty$ is handled by a finite truncation of z so that the condition

$$T = T_c(x), \quad \psi = AF(x), \tag{29}$$

is applied in the computational domain at $z = z_\infty < \infty$.

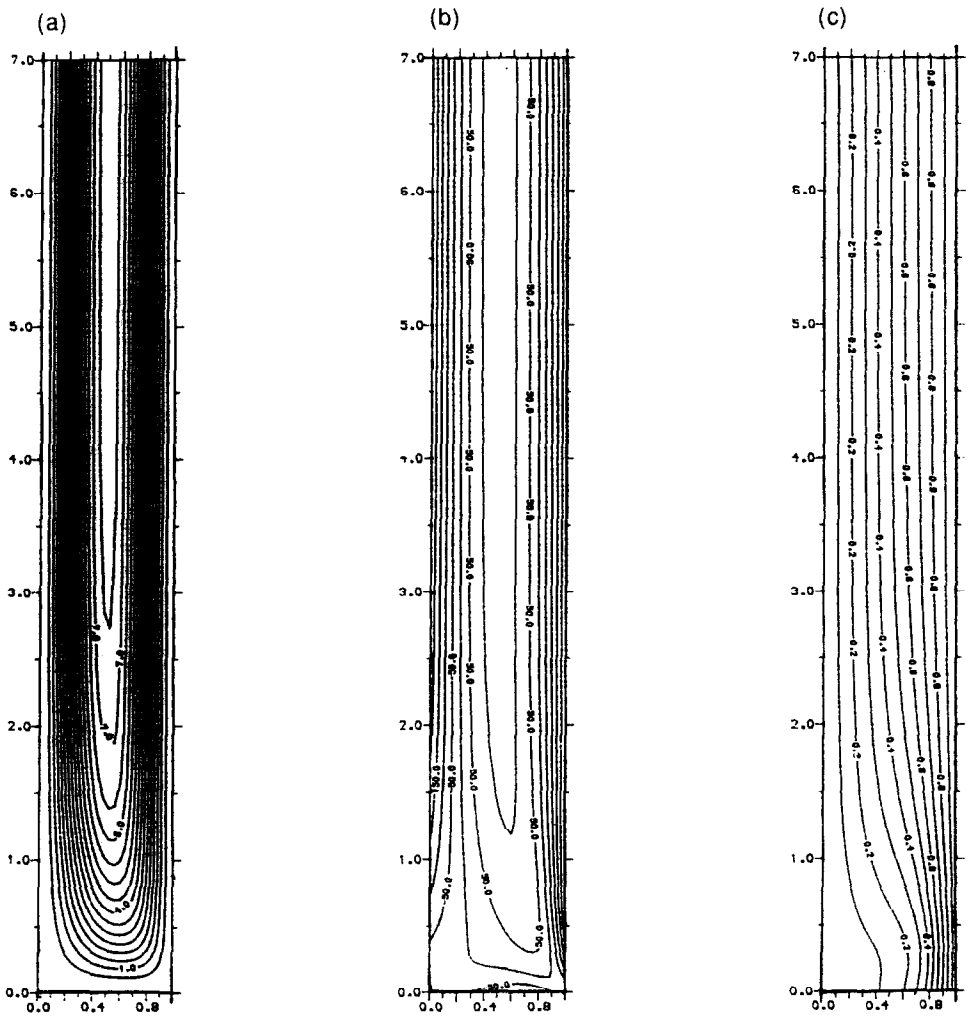

FIG. 6. Contours of the steady-state solution for (a) stream function, (b) vorticity, (c) temperature, for the insulating case with $\sigma = 0.733$ and $A = 3000$, using a 25×175 computational grid with $z_\infty = 7$.

It is then necessary to ensure that z_∞ is chosen sufficiently large that the computed solution does indeed approximate the actual solution of (20)–(28).

Some guidance on the choice of the outer boundary z_∞ is provided by results of an eigenvalue analysis of the outer condition (28) by Daniels [5]. This shows that the outer forms $T_c = x$ and $AF(x)$ are approached generally through a behaviour of the form

$$T \sim x + O(e^{-\mu z}), \quad \psi \sim A\{F(x) + O(e^{-\mu z})\} \quad (30)$$

as $z \to \infty$ where, for $A < A_c$, the leading eigenvalue μ has positive real part and for infinite Prandtl number varies from the value π at $A = 0$ to zero as $A \to \infty$, with

$$\mu \sim 2.58 \times 10^3 A^{-1} \quad (A \to \infty)$$

(Daniels [5]). This latter result indicates an e-folding decay length for the end-zone of $z \sim 3.88 \times 10^{-4} A$ so that for large values of A, the outer boundary of the computational domain must be increased accordingly.

The main interest is in the steady-state solution and the computation is stopped when the maximum difference between values of the solution at successive time steps is less than a specified tolerance, usually taken to be 10^{-6} for the temperature and vorticity fields. More details of numerical techniques involved in solving the whole system and of the effect of the grid size on the accuracy of solutions are discussed by Wang [11].

5. HEAT TRANSFER

The end-zones of the cavity play an important role in providing a correction to the conductive heat transfer associated with the core solution (17). The average heat flux for each wall of the end-zone is represented by

$$\alpha = \int_0^\infty \left(\left. \frac{\partial T}{\partial x} \right|_{x=0} - 1 \right) dz, \quad x = 0, \quad (31)$$

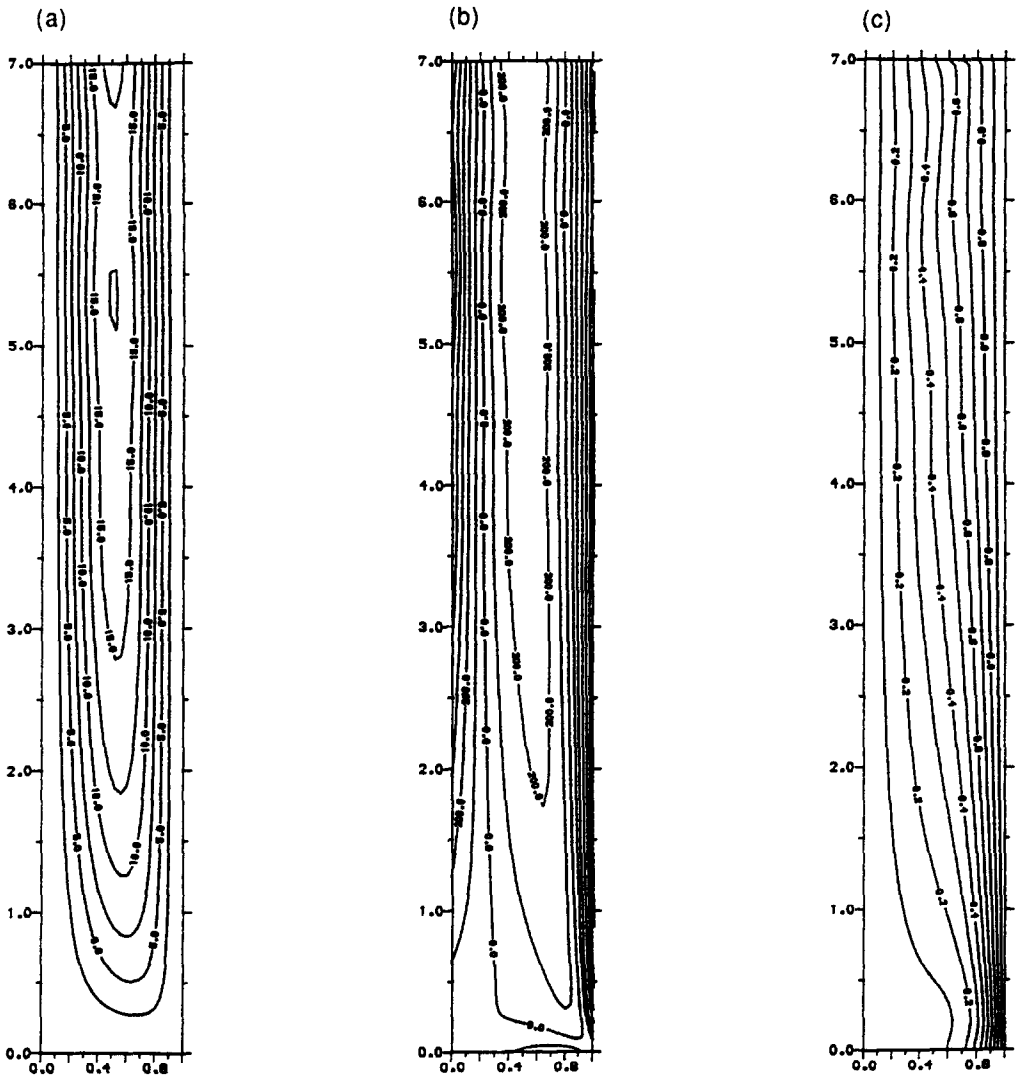

FIG. 7. Contours of the steady-state solution for (a) stream function, (b) vorticity, (c) temperature, for the insulating case with $\sigma = 0.733$ and $A = 7000$, using a 25×175 computational grid with $z_\infty = 7$.

$$\beta = \int_0^\infty \left(\left.\frac{\partial T}{\partial x}\right|_{x=1} - 1 \right) \mathrm{d}z, \quad x = 1, \tag{32}$$

$$\gamma = \int_0^1 \left.\frac{\partial T}{\partial z}\right|_{z=0} \mathrm{d}x, \quad z = 0, \tag{33}$$

where α and β represent contributions relative to a state of pure conduction. In the conducting case, integration of the energy equation (22) for steady-state motion in the end-zone and use of the boundary conditions (24) gives

$$\int_0^\infty \left(\left.\frac{\partial T}{\partial x}\right|_{x=1} - 1 \right) \mathrm{d}z - \int_0^\infty \left(\left.\frac{\partial T}{\partial x}\right|_{x=0} - 1 \right) \mathrm{d}z + \int_0^1 \left.\frac{\partial T}{\partial z}\right|_{z=\infty} \mathrm{d}x - \int_0^1 \left.\frac{\partial T}{\partial z}\right|_{z=0} \mathrm{d}x = A \int_0^1 F(x) \frac{\mathrm{d}T_c}{\mathrm{d}x} \mathrm{d}x \tag{34}$$

and use of (28) yields

$$\beta - \alpha - \gamma = \frac{A}{720}. \tag{35}$$

This relation can be used as a check on the accuracy of the computation. Simpson's rule is used to calculate the integrals (31)–(33).

In the insulating case, $\gamma = 0$ and the equation (35) becomes

$$\beta - \alpha = \frac{A}{720}. \tag{36}$$

Again, this relation can be used as a check on the accuracy of the computational solution. In addition, the values of α and β, together with the centrosymmetry of the flow, can be used to provide the overall Nusselt number for the cold wall of the cavity

$$Nu = \int_0^H \left.\frac{\partial \bar{T}}{\partial x}\right|_{x=0} \mathrm{d}z. \tag{37}$$

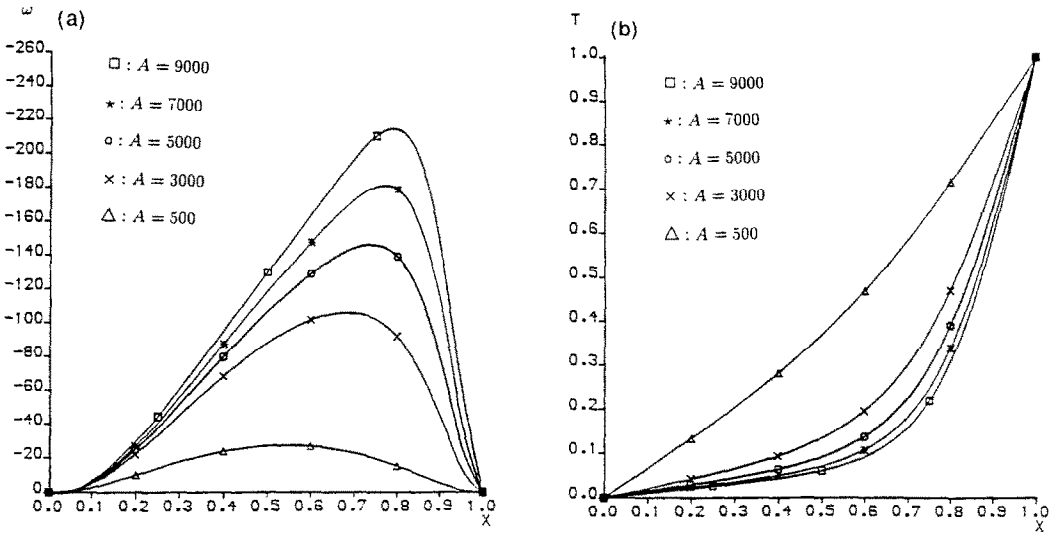

FIG. 8. The profiles of (a) skin friction and (b) temperature with $\sigma = 0.733$ for different Rayleigh numbers on the bottom wall for the insulating case.

This integral comprises three parts, arising from the main core contribution, where (17) applies, together with the convective corrections arising from each end zone. Thus

$$Nu = \int_0^{z_*} \left(\left. \frac{\partial \bar{T}}{\partial x} \right|_{x=0} - 1 \right) dz + \int_0^H dz + \int_{H-z_*}^{H} \left(\left. \frac{\partial \bar{T}}{\partial x} \right|_{x=0} - 1 \right) dz$$

but for a centro-symmetric steady-state solution the third integral evaluated within the upper end-zone can be replaced by an integral over the hot wall of the lower end-zone. Thus

$$Nu \sim \int_0^{z_*} \left(\left. \frac{\partial T}{\partial x} \right|_{x=0} - 1 \right) dz + \int_0^H dz + \int_0^{z_*} \left(\left. \frac{\partial T}{\partial x} \right|_{x=1} - 1 \right) dz, \quad (H \to \infty),$$

$$\sim H + \alpha + \beta, \quad (H \to \infty). \tag{38}$$

6. NUMERICAL RESULTS FOR AIR IN THE CONDUCTING CASE

Numerical results were obtained for a Prandtl number $\sigma = 0.733$ equivalent to that of air and for a range of Rayleigh numbers $500 \leqslant A \leqslant 9000$. For low Rayleigh numbers a 30×90 grid was used with an outer boundary $z_\infty = 3$, while for higher Rayleigh numbers, ($A \geqslant 3000$), a 25×175 grid was used with an outer boundary $z_\infty = 7$. In the numerical solution for low Rayleigh numbers it is relatively easy to achieve good accuracy and fast convergence to the steady state solution. At higher Rayleigh numbers accuracy is affected mainly by the formation of boundary layer structures near the walls and although accuracy can be improved by use of a finer grid, the smaller time step needed to maintain stability affects the rate of convergence. In general it is necessary to make a compromise in the choice of grid size and more sophisticated numerical techniques would be needed to treat the boundary layer structures which arise at very high Rayleigh numbers.

Contours of the steady state stream function, vorticity and temperature for different Rayleigh numbers are given in Figs. 1–3. These contours indicate that at low Rayleigh numbers ($A = 500$), the core solution is valid throughout most of the cavity except in roughly square areas near the ends where the flow turns direction. As the Rayleigh number increases, the nonlinearity of the end-zone flow gradually spreads vertically, and non-parallel flow occurs over an extended range of z, typically $0 < z < 4$ when $A = 5000$ (Fig. 2). At high Rayleigh numbers ($A > 5000$) the temperature field shows evidence of the development of a boundary-layer structure at the lower corner near the hot wall, which acts as a strong source of vorticity. Since buoyancy forces are proportional to the horizontal temperature gradient, this region produces vigorous convection up the hot wall, with most of the temperature variation occurring near the wall. Across the base region of the cavity, the isotherms are deflected towards the hot wall, indicating a tendency to align with the flow, characteristic of domination by convection in this part of the flow.

Figure 3 shows that when $A = 7000$ a multiple-cell structure begins to appear in the streamline field which at $A = 9000$ has developed to the stage where the outer boundary condition can no longer be applied consistently. These results are in good agreement with linear stability theory based on the breakdown of the parallel core flow. Small disturbances $\tilde{T}$ and $\tilde{\psi}$ of

arbitrary two-dimensional form are superimposed upon the basic state in the following manner:

$$T = x + \tilde{T}, \quad \psi = A(F + \tilde{\psi}). \tag{39}$$

The general solution of the linearised stability equations can then be written as a superposition of Fourier modes which for stationary convection take the form

$$(\tilde{\psi}(x,z), \tilde{T}(x,z)) = (\phi(x), \theta(x)) \exp(\mathrm{i}\tilde{\alpha}z) \tag{40}$$

where $\tilde{\alpha}$ is the vertical wavenumber. Thus

$$T = x + \theta(x) \exp(\mathrm{i}\tilde{\alpha}z), \tag{41}$$

$$\psi = A(F + \phi(x) \exp(\mathrm{i}\tilde{\alpha}z)), \tag{42}$$

where, from (20)–(22), θ and ϕ satisfy

$$\theta'' - \tilde{\alpha}^2\theta = -\mathrm{i}\tilde{\alpha}AF'\phi, \tag{43}$$

$$\phi'''' - 2\tilde{\alpha}^2\phi'' + \tilde{\alpha}^4\phi = \theta'$$

$$- \frac{\mathrm{i}\tilde{\alpha}A}{\sigma}\{(-\tilde{\alpha}^2F' - F''')\phi + F'\phi''\}. \tag{44}$$

From (24), (25) the appropriate boundary conditions are

$$\theta = \phi = \phi' = 0 \quad \text{on} \quad x = 0, 1. \tag{45}$$

The system (43)–(45) has been previously considered by Vest and Arpaci [2], Hart [12], Korpela *et al.* [3], Bergholz [4] and more recently by Daniels [5]. Real values of the wavenumber, corresponding to multi-cellular convection, occur for Rayleigh numbers $A > A_c(\sigma)$ where $A_c \approx 7880\sigma$ and the corresponding critical value of the wavenumber is $\tilde{\alpha}_c \approx 2.8$. As explained by Daniels [5], the multi-cellular motion is actually forced to occur as part of the steady state solution in the end-zone, since the eigenvalue corresponding to $\tilde{\alpha}_c$ is one of the infinite family of eigenvalues generated by the need for the end-zone solution to adjust from the parallel core flow to the boundary conditions (23)–(27).

The appearance of secondary vortices at $A = 7000$ in Fig. 3 is consistent with the fact that $A_c = 5776$ when $\sigma = 0.733$ and the wavelength $z \approx 2$ is reasonably consistent with the critical wavelength $2\pi/\tilde{\alpha}_c = 2.24$ predicted by the linear stability analysis.

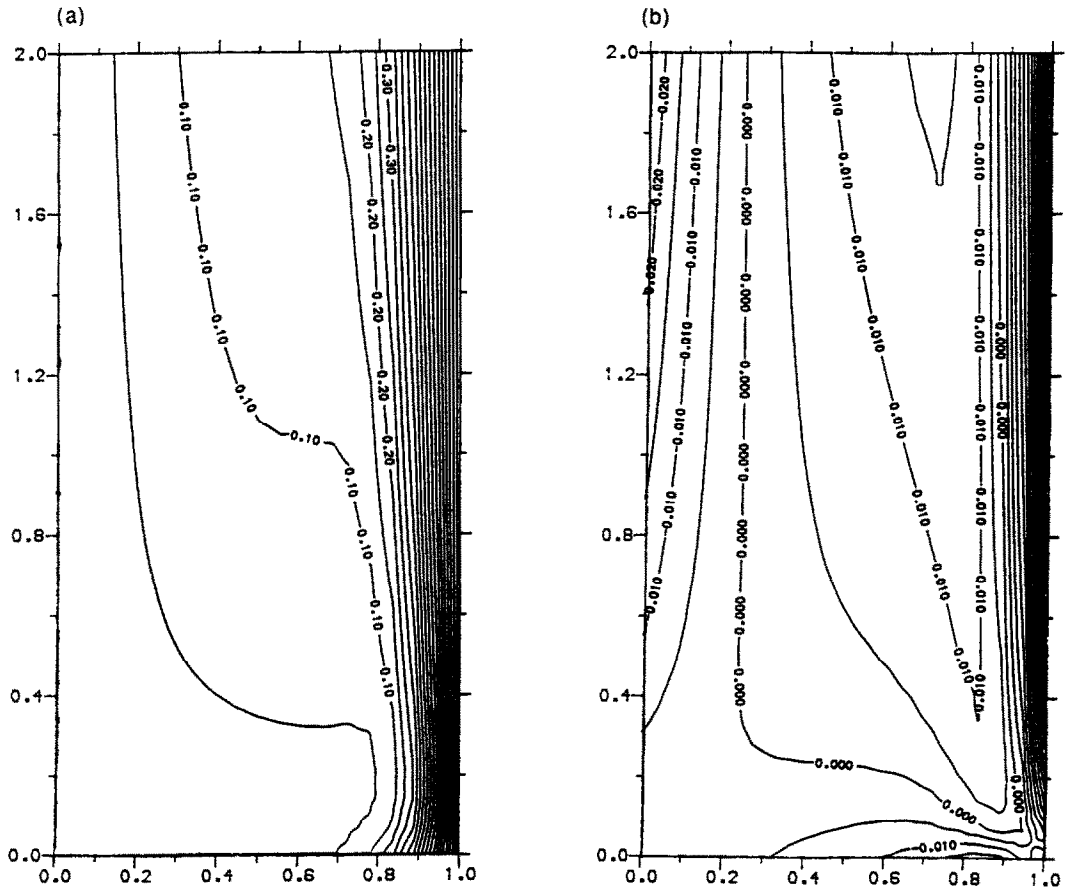

FIG. 9. Contours of the steady-state solution for (a) temperature, (b) vorticity, near the bottom of the slot for the insulating case with $\sigma = 6.983$, $A = 30\,000$ and $z_\infty = 30$.

The local Nusselt number on the bottom wall is shown for various values of the Rayleigh number in Fig. 4.

7. NUMERICAL RESULTS FOR AIR IN THE INSULATING CASE

Numerical results were obtained for air ($\sigma = 0.733$) for a wide range of Rayleigh numbers, equivalent to the range for the conducting case considered in the previous section. The grid sizes and the outer boundaries were the same as those described in the previous case, and the accuracy and convergence of the solutions followed a very similar pattern. The steady-state flow patterns are illustrated in Figs. 5–7 by contours of stream function, vorticity and temperature for Rayleigh numbers ranging from 500 to 7000. As expected, the transition from conductive flow at low Rayleigh number to convective flow at high Rayleigh number is similar to that observed in the case of conducting boundaries, except near the base where the isotherms are free to shift towards the hot wall, convected by the turning motion of the fluid. The streamlines show that at $A = 500$, the flow pattern is nearly symmetric, but at higher Rayleigh numbers there is asymmetry caused by the accentuated upward motion near the hot wall, associated with the formation of a thermal boundary layer there. The vorticity fields also show that strong horizontal vorticity gradients are set up near the hot wall resulting in vigorous convection there. When A reaches the critical Rayleigh number $A_c \approx 7880\sigma$ (see Fig. 7), the parallel flow approaching the core is replaced by multicellular convection, as in the computations of the previous section and the wavelength is again consistent with that predicted by the linear stability theory. The end-zone solution can no longer be treated in isolation, the outer boundary condition (28) is inconsistent, and a multiple-cell structure occurs in the whole slot. Figure 8 shows the skin friction and temperature on the bottom wall, indicating how asymmetry develops as the Rayleigh number increases. This behaviour is consistent with the change of the flow pattern observed in Figs. 5–7, the skin friction maximum and the thermal gradient shifting considerably towards the hot wall.

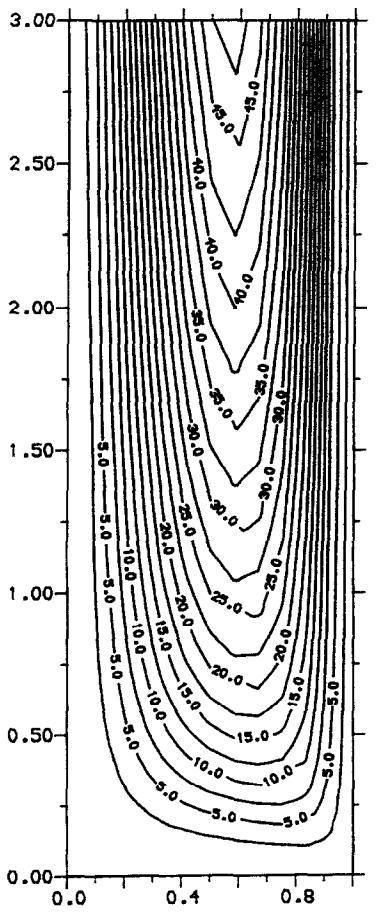

FIG. 10. Contours of stream function near the bottom of the slot for the insulating case with $\sigma = 6.983$, $A = 40\,000$ and $z_e = 50$.

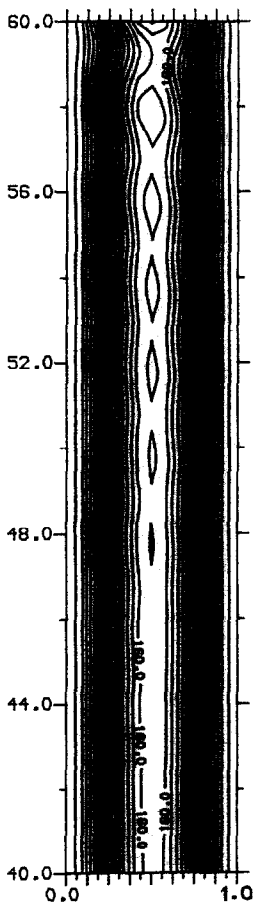

FIG. 11. Streamlines near the top of the end-zone for the insulating case with $\sigma = 6.983$.

Table 1. Comparison of the two sides of equation (36) for air

A	$\beta-\alpha$	$A/720$	Discrepancy
500	0.691	0.694	0.003
3000	4.092	4.167	0.075
5000	6.75	6.955	0.194

On the cold wall, the local Nusselt number increases in the z direction, and decreases as A increases. A region with a very weak horizontal temperature gradient then exists near the corner of the cold wall where the heat transfer is relatively small. On the hot wall, there are strong horizontal temperature gradients and the heat transfer reaches a maximum value near the bottom of the wall and then decreases along the z direction. The local Nusselt number for the hot wall increases with A, as more heat is transferred into the upward-moving fluid. Most of this heat is conveyed, via the core, to the end-zone at the top of the cavity, where it leaves through the cold wall. This process is represented by the steady-state integral of the energy equation $\beta-\alpha = A/720$ obtained in (36), the right-hand side being a measure of the heat flux conveyed through the core region. This result was used to test the accuracy of the numerical computations, as shown in Table 1. This shows good consistency and for higher Rayleigh numbers the discrepancy increases as it becomes more difficult to adequately resolve the solution.

The overall Nusselt number Nu is obtained from (31)–(38) and the numerical results are listed in Table 2 for three values of the Rayleigh number. The results show good agreement with previous numerical calculations for the whole cavity by Lee and Korpela [6] and Raithby and Wong [13], and also compare well with the experiments of El Sherbiny *et al.* [14]. It should be noted that the numerical results of the end-zone computation for one pair of the parameters A and σ can be used to provide approximations to the Nusselt number for all aspect ratios H provided H is sufficiently large for the conductive regime to apply in the core. This is a significant advantage of the asymptotic method adopted here.

8. NUMERICAL RESULTS FOR WATER IN THE INSULATING CASE

Numerical results were obtained for water ($\sigma = 6.983$) for a wide range of Rayleigh numbers varying from 500 to 70 000. The outer boundaries used in the computations varied from 3 to 60, and various grid sizes were used according to the value of the Rayleigh number. Unlike the case of air, much higher Rayleigh numbers were considered here, so that much larger outer boundaries were needed and grid sizes ranged from 30×90, 25×175 and 18×280 to 12×600. Most of the computations for high Rayleigh numbers were based on the use of solutions for lower Rayleigh number as the initial states, thereby reducing the computational time needed.

Contours of stream function, vorticity and temperature, showing some detailed results for the fields near the bottom wall are presented in Figs. 9 and 10 for Rayleigh numbers $A = 30\,000$ and 40 000, which are below the critical Rayleigh number for stationary transverse rolls

$$A_c \approx 7880\sigma = 55\,049$$

predicted by linear stability theory. These graphs provide detailed information about the flow structure of water in the end regions of the cavity; because instability is delayed to much higher Rayleigh numbers when the Prandtl number is large, the nonlinear development of the flow can be followed much further than for the case of air.

As the Rayleigh number increases, the region of nonparallel flow near the base of the cavity spreads upwards and for values of A up to 7000 the flow near the base is very similar to that for air shown in Figs. 5–7. As A increases further the isotherms near the lower corner are compressed towards the hot wall leading to an almost isothermal region over most of the base and except near the hot wall, the flow near the base of the cavity is dominated by convection. For $A = 30\,000$, where the outer boundary is taken at $z_\infty = 30$, a detailed picture of the flow near the base (Fig. 9) shows how the 0.05 isotherm follows the streamline pattern before being deflected sharply to the bottom boundary in the region $z \leqslant 0.4$. Near the hot wall, the region $0.8 < x < 1$, $0 \leqslant z \leqslant 2$ shows

Table 2. Comparison of the average Nusselt number Nu/H on the cold wall as given by (38) with previous results for air

Method	Researchers	A	H				
			5	10	15	20	40
Numerical	Present study	500	1.031	1.0155	1.0103	1.0077	1.0039
Numerical	Present study	3000	1.41	1.205	1.1367	1.102	1.0512
Numerical	Lee and Korpela [6]	3000	1.39	1.17	1.129	1.08	1.043
Numerical	Raithby and Wong [13]	3000	1.40	1.2		1.13	1.045
Experimental	El Sherbiny *et al.* [14]	3000				1.07	1.01
Numerical	Present study	5000	1.732	1.366	1.244	1.183	1.0915
Numerical	Lee and Korpela [6]	5000	1.62	1.338	1.235	1.165	1.08
Experimental	El Sherbiny *et al.* [14]	5000				1.17	1.04

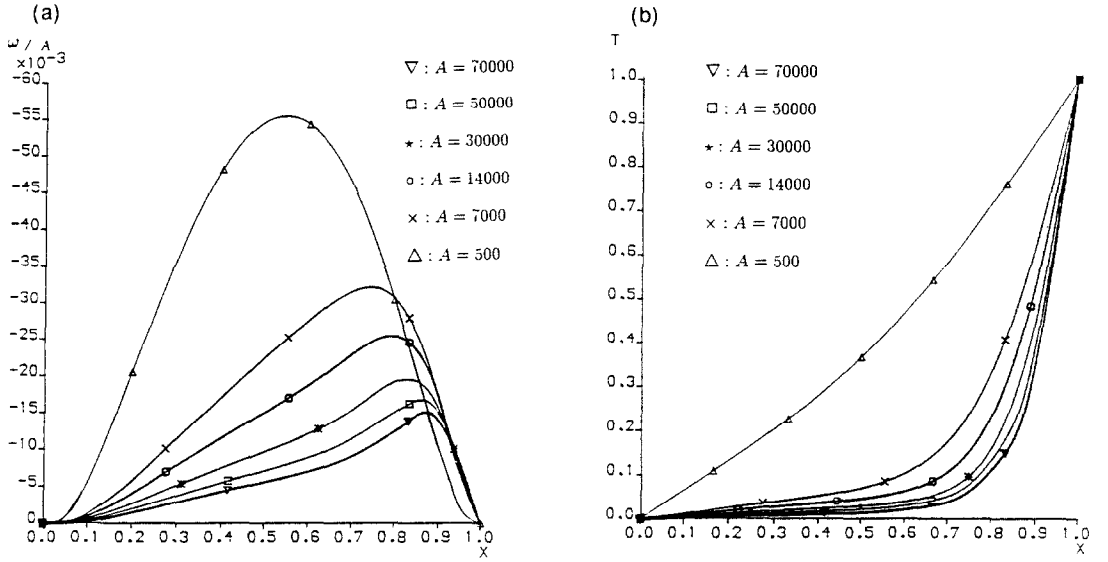

FIG. 12. The profiles of (a) skin friction ω/A and (b) temperature, with $\sigma = 6.983$ for different Rayleigh numbers on the bottom wall for the insulating case.

tightly-packed isotherms indicating strong horizontal temperature gradients and the formation of a vertical thermal boundary layer. The local heat transfer into the system is a maximum near the base of the hot wall. The vorticity field shows a complex structure near the lower, hot corner and a region of maximum vorticity near the hot wall associated with the vertical boundary layer. Figure 10 shows the streamline pattern for $A = 40\,000$.

When A reaches 60 000 the parallel flow region at the outermost part of the end-zone becomes susceptible to minor oscillations, consistent with a critical Rayleigh number $A_c \approx 55\,000$. The corresponding critical wavenumber predicted by linear stability theory is $\tilde{\alpha}_c \approx 2.8$ (Vest and Arpaci [2], Bergholz [4]), equivalent to a wavelength $z = 2\pi/\tilde{\alpha}_c \approx 2.24$ between the centres of neighbouring, co-rotating cells. This compares well with a value of about 2.1 obtained by the present calculations. At $A = 70\,000$ the multiple cell structure becomes clearly established along the centre-line of the parallel flow region, as shown in Fig. 11.

Figure 12 shows the skin friction and the temperature on the bottom wall. At low Rayleigh number ($A = 500$) the temperature profile is approximately linear and as A increases the major variation shifts to the neighbourhood of the hot wall, with most of the base of the cavity then at the temperature of the cold wall. This is consistent with the large Rayleigh number structure at infinite Prandtl number proposed by Daniels [5, 7]. The numerical computations described here are broadly consistent with the main features of this structure, including the existence of an outer zone of vertical extent $O(A)$, which allows adjustment to the parallel core flow, and a thin horizontal layer of height $O(A^{-1/4})$ which is dominated by convection and feeds fluid into the base of a vertical boundary layer on the hot wall. The Prandtl number of the computations is actually large but finite so as A increases the end-zone problem in fact no longer has a consistent solution when A exceeds $A_c \approx 55\,000$.

REFERENCES

1. G. K. Batchelor, Heat transfer by free convection across a closed cavity between vertical boundaries at different temperatures, *Q. J. Appl. Math.* **12**, 209–233 (1954).
2. C. M. Vest and V. S. Arpaci, Stability of natural convection in a vertical slot, *J. Fluid Mech.* **36**, 1–15 (1969).
3. S. A. Korpela, D. Gozum and C. B. Baxi, On the stability of the conductive regime of natural convection in a vertical slot, *Int. J. Heat Mass Transfer* **16**, 1683–1690 (1973).
4. R. F. Bergholz, Instability of steady natural convection in a vertical slot, *J. Fluid Mech.* **84**, 743–768 (1978).
5. P. G. Daniels, Transition to the convective regime in a vertical slot, *Int. J. Heat Mass Transfer* **28**, 2071–2077 (1985).
6. Y. Lee and S. A. Korpela, Multicellular natural convection in a vertical slot, *J. Fluid Mech.* **126**, 91–121 (1983).
7. P. G. Daniels, Convection in a vertical slot, *J. Fluid Mech.* **176**, 419–441 (1987).
8. A. E. Gill, The boundary-layer regime for convection in a rectangular cavity, *J. Fluid Mech.* **26**, 515–536 (1966).
9. P. J. Roache, *Computational Fluid Dynamics*. Hermosa, Alberquerque, NM (1976).
10. A. Brandt, Multi-level adaptive solutions to boundary-value problems, *Math. Comp.* **31**, 333–390 (1977).
11. P. Wang, Thermal convection in slender laterally-heated cavities, Ph.D. Dissertation, City University, London (1992).
12. J. E. Hart, Stability of the flow in a differentially heated inclined box, *J. Fluid Mech.* **47**, 547–576 (1971).
13. G. D. Raithby and H. H. Wong, Heat transfer by natural convection across vertical air layers. *Numer. Heat Transfer* **4**, 447–457 (1981).
14. S. M. El Sherbiny, G. D. Raithby and K. G. T. Hollands, Heat transfer by natural convection across vertical and inclined air layers, *Trans. A.S.M.E. J. Heat Transfer* **104**, 96–102 (1982).